

**Direct breaking of the internal tide near topography:
Kaena Ridge, Hawaii**

JODY M. KLYMAK¹, ROBERT PINKEL², AND LUC RAINVILLE³

¹*University of Victoria, Victoria, B.C.*

²*Scripps Institution of Oceanography, La Jolla CA*

³*Woods Hole Oceanographic Institution, Woods Hole MA*

Submitted, *Journal of Physical Oceanography*, April 17, 2007

April 17, 2007

Corresponding author address:

J. Klymak, School of Earth and Ocean Sciences, University of Victoria, P.O. Box 3055
STN CSC, Victoria, B.C., Canada, V8W 3P6, jklymak@uvic.ca

ABSTRACT

Barotropic to baroclinic conversion and attendant phenomena were recently examined at the Kaena Ridge as an aspect of the Hawaii Ocean Mixing Experiment. Two distinct mixing processes appear to be at work in the waters above the 1100-m deep ridge crest. At mid-depths, above 800 m, mixing events resemble their open ocean counterparts. There is no apparent modulation of mixing rates with the fortnightly cycle and they are well-modeled by standard open-ocean parameterizations. Nearer to the topography, there is quasi-deterministic breaking associated with each baroclinic crest passage. Large amplitude small-scale internal waves are triggered by tidal forcing, consistent with lee wave formation at the ridge-break. These waves have vertical wavelengths on the order of 400-m. During spring tides the waves are non-linear and exhibit convective instabilities on their leading edge. Dissipation rates exceed those predicted by the open-ocean parameterizations by up to a factor of 100, with the disparity increasing as the seafloor is approached.

These observations are based on a set of repeated CTD and microconductivity profiles obtained from the *R/P FLIP* which was tri-moored over the southern edge of the ridge crest. Ocean velocity and shear was resolved to 4-m vertical scale by a suspended Doppler sonar. Dissipation was estimated both by measuring overturn displacements and from microconductivity wavenumber spectra. The methods agreed deeper than 200 m where sensor resolution limitations do not limit the turbulence estimates. At intense mixing sites new phenomena await discovery and existing parameterizations cannot be expected to work.

1. Introduction

As the barotropic tide forces stratified water over topography, energy is lost principally in the generation of baroclinic waves (Merrifield and Holloway 2002; Klymak and Gregg 2004). The dissipation of these waves plays a significant role in determining the geography of mixing in the ocean. Here we address dissipation mechanisms prevalent at a generation site in the Hawaiian Ridge, in the waters directly above the Kaena Ridge.

The dissipation of the barotropic tide in the deep ocean is generally discussed in terms of three mechanisms:

1. Direct bottom friction;
2. Internal tide generation with subsequent decay via non-linear interactions with the ambient internal wave field (St. Laurent and Garrett 2002; Polzin 2004), perhaps enhanced at low latitudes by subharmonic instabilities (MacKinnon and Winters 2005; Hibiya and Nagasawa 2004);
3. Internal tide radiation with distant breaking as it encounters far-field topography (Legg and Adcroft 2003; Johnston and Merrifield 2003; Nash et al. 2004).

Here we highlight a fourth pathway

4. Internal tide instability and breaking in the immediate proximity of the generating region.

This is a well-known energy sink in tidal flows in fjords (Freeland and Farmer 1980; Klymak and Gregg 2004; Inall et al. 2005). The discovery of this phenomenon in the deep sea has awaited the development of rapid-sampling, precise sensors. Direct breaking is a consequence of super-critical flow associated with the baroclinic tide at the generation site. The exact mechanism of super-criticality depends on a number of parameters – the aspect ratio of the topography relative to the internal waves, the width

of the obstacle relative to the tidal excursion, and the strength of the flow relative to the obstacle height and stratification (Baines 1995; Garrett and Kunze 2007).

This paper presents turbulence dissipation measurements made at Kaena Ridge, an important internal-tide generation site on the Hawaiian Ridge (Rudnick et al. 2003). The site, between the islands of Kauai and Oahu, has been shown to generate a significant internal tide (Lee et al. 2006; Rainville and Pinkel 2006; Nash et al. 2006; Martin et al. 2006), in agreement with numerical model estimates (Merrifield and Holloway 2002). In-situ dissipation estimates indicate that between 5 and 25% of the power lost from the barotropic tide goes into local dissipation processes (Klymak et al. 2006). The large spread of this estimate indicates the difficulty in measuring turbulence dissipation over such a large area.

Given the tidal origin of the internal waves, we might expect a spring-neap cycle to the turbulence dissipation as found in fjord studies and in the Brazil Basin (St. Laurent et al. 2001). However, time-series of turbulence dissipation made a modest distance away from the generation site (at various depths, about 2500 m off-ridge) varied by only a factor of two with the spring-neap cycle (Klymak et al. 2006). In contrast, near-bottom dissipation estimates from moorings on the slopes of the Hawaiian Ridge demonstrate a strong spring-neap cycle to the dissipation (Levine and Boyd 2006). These mooring measurements also show that the dissipation is phase-locked to the semi-diurnal tidal cycle in a predictable manner (Levine and Boyd 2006; Aucan et al. 2006). Presumably, the mechanism that drives turbulence near the sea-floor is different from that further aloft.

The measurements in this paper are taken atop the Ridge from *R/P FLIP*. We estimate the turbulence dissipation at our site via two independent indirect methods (section 2). A clear distinction is seen between the near-bottom, tidally modulated turbulence dissipation and the more steady dissipation away from the bottom (section 3). We postulate that there are two regimes, a direct instability of the internal tide near the ridge crest, and a less-direct midwater energy cascade through the broadband internal wavefield (section 4). Our measurements compare well with other measurements

made at the ridge (section 5) and help explain the discrepancy in the observations cited above.

2. Measurements

a. Site description

The measurements were collected from the *R/P FLIP*, which was moored in 1100 m of water at the south edge of Kaena Ridge, between Oahu and Kauai (Fig. 1). FLIP was deployed for 35 days as part of the Hawaiian Ocean Mixing Experiment (HOME) along a line occupied by two other moorings “Big Boy” (Levine and Boyd 2006) on the north flank and “DS” (Aucan et al. 2006) on the south. Here we analyze data from 25 days of optimal working conditions comprising the large part of two spring and neap tides (Fig. 2, see Rainville and Pinkel (2006) for further details).

FIG. 1

R/P FLIP was instrumented with a Doppler sonar that had 4 upward and 4 downward looking beams that was deployed at 418 m. This was able to measure water velocity from as near to the surface as side-lobe interference would allow (about 60 m depth), to 800 m. The four up-looking beams transmitted at 170 kHz, while the down-looking beams transmitted at 140 kHz. Depth resolution was 4-m. There was persistent interference at 550 m depth where the sea-floor echo from a previously transmitted pulse was received by the sonar. There were no usable data between 412 and 424 m due to ringing of the sonar transmit pulses immediately following transmission.

FIG. 2

Two conductivity and temperature versus depth (CTD) packages were deployed, one cycling between 10 and 400 m depth and the second between 400 and 800 m. Cycles were made at synchronous 4-minute intervals with a drop speed of 3.5 ms^{-1} . The conductivity and temperature cells on the SBE 9-11 CTDs were matched by linearly shifting the conductivity time series back by either 0.1353 s or 0.0658 s (one of the CTDs was replaced Sept 26, 2002, and had the shorter lag). It is not necessary to correct for thermal lag in such stratified waters. The 24 Hz density data was

then smoothed by 15 points, or 2.188 m. Temperature data is not as noisy, and was smoothed to 16 Hz, or 0.2 m.

Both CTDs were initially equipped with SBE 7-02 micro-conductivity sensors on the nose, sampled at 96 Hz. The upper CTD was lost on Sep. 24, and replaced with a Seabird 9/11 plus which did not have a micro-conductivity sensor. On Oct. 8 the deep micro-conductivity sensor failed so we do not present data after that date. To estimate turbulent dissipation rates, we calculated wavenumber spectra of microconductivity and surveyed macroscale regions of statically unstable water (overturns), as described next.

b. Overturn estimates of dissipation

The turbulence dissipation rate ϵ can be estimated from density overturns (Thorpe 1977; Alford and Pinkel 2000b). For each profile of temperature and salinity, potential density is calculated relative to 200 m for the upper CTD and 600 m for the lower. When density inversions are encountered, the Thorpe displacement is then given by the difference in depth of the water parcel in the unsorted and sorted profiles (ρ_s):

$$L_\rho = z(\rho) - z(\rho_s).$$

The bounds of an overturn are determined as where the sum of L_ρ drops back to zero (Fig. 3b). The stratification appropriate to each overturn was calculated as

$$N_T^2 = \left(\frac{g}{\rho} \right) \frac{\max(\rho) - \min(\rho)}{\max(z) - \min(z)}$$

where the maxima and minima are across the overturn. This gives an estimate for the turbulence dissipation rate:

$$\epsilon_\rho = aL_\rho^2 N_T^3, \quad (1)$$

where $a \approx 1$ is a constant of proportionality (Dillon 1982; Moum 1996b). For comparison, the same procedure is carried out for potential-temperature to get ϵ_θ .

The overturning method has some clear disadvantages, particularly for a probe moving through the water at 3.5 ms^{-1} . The smoothing required for density preci-

sion limits detectable overturns to scales > 2 m. This hampers our investigation in the highly-stratified water in the upper 150 m. Temperature overturns are not usable where salinity compensates temperature, which occurs in a number of places in the data set, particularly near the surface. Nonetheless, for large parts of the cruise, the temperature and density overturning methods agree with each other, and with the micro-conductivity and internal wave estimates, giving confidence that we have a useful estimate of the turbulence dissipation rate.

FIG. 3

c. Microconductivity estimates of dissipation

The micro-conductivity sensors are corrected for a pre-emphasis filter applied in the circuitry (Alford and Pinkel 2000a). The gain and offset of the sensors is calibrated *in-situ* by matching with the CTD macro sensor at low vertical wavenumbers (Fig. 4). These offsets were recalculated at 48-h intervals. Calibration shifts were mainly associated with removing the CTDs from the water. For the data presented here the *in-situ* calibration does not drift by more than 20% from the factory calibration.

FIG. 4

The method here generally follows that of (Alford and Pinkel 2000a) and Klymak and Moum (2007). To relate conductivity to turbulence dissipation, first assume that conductivity fluctuations primarily reflect temperature fluctuations. Conductivity actually depends on both temperature (T) and salinity (S):

$$\frac{dC}{dz} = a^{-1} \frac{dS}{dz} + b^{-1} \frac{dT}{dz}$$

where a and b are local constants. At 35 psu and 10°C are $a \approx 10.9 \text{ S}^{-1} \text{ m psu}$, and $b \approx 11.1 \text{ S}^{-1} \text{ m K}$. Since a and b are approximately the same size our assumption, that

$$\frac{dC}{dz} \approx b^{-1} \frac{dT}{dz},$$

is only valid when $dT/dS \gg 1$. This is a valid assumption through most of the water column, where $dT/dS > 5$ (Fig. 5b). This approximation allows us to estimate the temperature spectrum from the conductivity spectra $\phi_T \approx b^2 \phi_C$.

FIG. 5

Temperature spectra are related to turbulence dissipation by the Osborn-Cox assumption: $K_\rho = \Gamma \varepsilon / N^2$, where N^2 is the local stratification, and $\Gamma \approx 0.2$ is a mixing efficiency (Osborn 1980; Moum 1996a). Assuming that the turbulence results in the same Fickian diffusion of temperature as it does of density, then $K_\rho = K_T$. K_T is estimated from the temperature-derivative spectrum by the Batchelor spectrum (Batchelor 1959):

$$\Phi_{dT/dz} = 2K_T \left\langle \frac{dT}{dz} \right\rangle^2 (C_T \varepsilon^{-2/3} \alpha_z^{1/3} + q \varepsilon^{-1/2} \alpha_z), \quad (2)$$

where $\alpha_z = 2\pi k_z$ is the radian wavenumber, $C_T \approx 0.44$ is the Monin-Corrsin constant and $q = 2.3$ is the strain rate of the turbulence. Here we have followed Klymak and Moum (2007) in the choice of constants, and in adding the spectra. We have also ignored the high-wavenumber roll-off because it is not resolved.

In order to estimate ε , $K_T = \Gamma \varepsilon N^{-2}$ is used in equation (2), where N^2 is a local estimate of the stratification. For ε to be the only unknown, estimates of the local temperature and density gradients are needed. These can be evaluated independently, however, doing so increases the noise in the estimates, particularly in the low-stratification water and in the presence of overturns. This is avoided by calculating the temperature gradient from the stratification:

$$N^2 = \alpha g \frac{dT}{dz} (1 + 1/R_\rho), \quad (3)$$

where R_ρ is the density ratio. So equation (2) can be rewritten as

$$\Phi_{dT/dz} = \frac{2\Gamma N^2}{\left(g\alpha(1 + R_\rho^{-1})\right)^2} \varepsilon (C_T \varepsilon^{-2/3} \alpha_z^{1/3} + q \varepsilon^{-1/2} \alpha_z). \quad (4)$$

Temperature spectra were calculated from the microconductivity probe over 1-s patches of data (96 points, or 3.6 m). At low wavenumbers, the spectra are dominated by internal waves and other finescale motions. At high wavenumbers the imprecision of the sensor response correction dominates the signal. Therefore, equation (4) was fit over a limited wavenumber range $4 < k_x < 9$ $\text{cyc. } m^{-1}$ (Fig. 6). The actual calculation is carried out on short spectra (16 points) averaged in 1-s bins, considerably increasing

the stability of the estimate from bin to bin. N^2 is calculated from the same density signal used for the overturning analysis.

FIG. 6

d. Sensitivity of dissipation rate estimates

The two methods of estimating the dissipation are compared extensively below, both with each other and with shear-probe microstructure measurements made at the ridge (Carter et al. 2006). Here a preliminary comparison is made for two depth intervals, one shallow and one deep, during the first spring tide (Fig. 7). The results, which will also be apparent below, indicate that the two methods agree very well in deep water (Fig. 7c and d). The overturning method misses small dissipation events because the 2.2-m smoothing of the density signal. However, the mean is dominated by large dissipation rates, and the estimates agree in the mean. Shallower, the stratification increases and the resolution of the CTD is not adequate to resolve overturns, and the mean dissipation rate is under-predicted by a factor of 5 (Fig. 7a and b), relative to the estimates derived from the microconductivity cell.

FIG. 7

The reason the overturning method ϵ_ρ misses overturns is because the outer length scale of the turbulence, the Ozmidov scale $L_O = 2\pi (\epsilon N^{-3})^{1/2}$, is less than the smoothing scale of the CTD data, 2.2 m. This is borne out by comparing how much of the water column has $L_O > 2.2$ m (as determined from the microconductivity estimates) and how much has detectable overturns (Fig. 8). The same percentages apply to both metrics of turbulence, and show why the shallow, highly stratified data misses a large proportion of the turbulent events.

FIG. 8

The 2.2-m smoothing of the density data was chosen to give the most-appropriate match between the two estimates at mid-depths (Fig. 9). If there is no smoothing, then the overturn method overestimates everywhere (Fig. 9a). Increasing the smoothing of the density data decreases the average dissipation, but does so most dramatically at shallow depths. Deeper than 250 m, data are relatively unaffected by the smoothing. Similar comparisons on other time periods show even better agreement deeper that

250 m with the 2.2-m smoothing, so we have used that for calculating ϵ_p . In the rest of the paper we compare the “overturn” and “spectral” estimates both spatially and temporally. They are also compared with dissipation profiles collected by Carter et al. (2006) using a free-fall microstructure (shear-probe) profiler.

FIG. 9

3. Observed Dissipation

The strongest turbulence at our site is found near the bottom of our profiling range, and linked to the local internal tide waveform. Further aloft, turbulence is weaker and not as time-dependent. We demonstrate this with representative data.

a. Example time periods

First, three example records are presented. A 1.5-day sample from neap tide and two 1.5-day periods from the two spring tides are chosen.

The neap tide example has isopycnal excursions of over 50 m near the bottom (Fig. 10a), rising just before the peak velocity at that depth. Tidal phase is propagating downwards at about 600 m in 3 h, indicative of upwards propagating energy. There is also evidence of near-inertial waves (Pinkel 2006). The third tidal peak is somewhat larger than the other two, and has a sharp rebound at approximately 17 Sep 2002, 05:00. This rebound is a consistent feature of the near-bottom tidal response during strong forcing.

FIG. 10

The strongest turbulence in this example is in this third crest (Fig. 10b,c). There is a small burst during the first crest, and a smaller one concentrated in a thin sheet in the second one. Higher in the water column, mixing is weaker and sporadic, taking place in sheets that last for a few hours each.

The two methods of estimating the turbulence dissipation rate appear to agree quite well at most depths (Fig. 11a,b). The micro-conductivity method ϵ_χ is a little higher near 600 m, mostly due to two thin tendrils near Sep. 18, 1500. The magnitude of

ϵ_p is diminished above 250 m, where the stratification is stronger. Here overturns are smaller and sensor resolution becomes a factor.

FIG. 11

The spring tide on Sep 20 is more energetic and exhibits greater dissipation (Fig. 12). Isopycnal excursions exceed 100 m at 800 m depth. Again, there is downward phase propagation of the velocity signal, with the deeper flow lagging the barotropic velocity predicted from the Oregon State Tidal Simulation (OTIS Egbert and Erofeeva 2002) by almost three hours. Isopycnals near the bottom of the record are asymmetric, with the leading edge rising more sharply than the trailing edge drops. The second wave has a sharp rebound at the top between 500 and 700 m that shows a downward phase propagation. This rebound is seen in other waves in the time series, though not on every cycle.

The on-ridge flow and heaving isopycnals are associated with strong turbulence deeper than 400 m in all three waves. Regions of turbulence 50–100 m thick last for hours, often tracking isopycnals. The regions appear predominantly phase-locked to the rising edge of each crest. In comparison to the neap tide, the water below 500 m is more turbulent by a factor of four or five. Higher in the water column there is very little difference.

FIG. 12

A stronger flood tide from later in the cruise shows larger isopycnal excursions, exceeding 150 m near the bottom (Fig. 13; note that this plot is only of the bottom 400 m). There are sharp high-frequency vertical undulations, almost 50 m, at the peaks of each tide. Again, the internal tide is asymmetric near the bottom, with the leading edge steeper than the trailing, reminiscent of an internal bore. Overturns on the leading edges can be clearly seen in the contours, even at this coarse contouring interval. Inspection of individual profiles reveals overturns exceeding 120 m height. During the on-slope phase of the internal tide, average ϵ below 400 m is of order $\epsilon \approx 10^{-7} \text{ m}^2\text{s}^{-3}$, with most of that in more dissipative bursts exceeding $\epsilon \approx 10^{-6} \text{ m}^2\text{s}^{-3}$. The trailing edges of the waves are not turbulent except in isolated tendrils.

FIG. 13

b. Detailed overturn

An expanded view of the velocity, temperature, and turbulence fields during a strong on-ridge tide demonstrates a rich array of features (Fig. 14). The strongest (modeled) barotropic on-ridge flow is at about 08:00. The baroclinic response lags by an hour, with a clear downward phase propagation. The water column above 500 m, exhibits weak waves and few overturns. Deeper than 500 m, there are three regions with strong turbulence and clear overturns. The first occurs just as the barotropic tide is reversing direction (05:00). The leading edge of this region has small overturns but strong stratification, leading to dissipation values in excess of $10^{-6} \text{ m}^2 \text{ s}^{-1}$. These overturns manifest themselves as small tufts in the weakly stratified water above. This first patch has strong turbulence following isopycnals for over an hour.

The second patch of turbulence occurs at the leading edge of deeper isopycnals just after 06:00. This is a weakly stratified region, with almost 150-m tall overturns. This strong turbulence lasts for a little less than one hour. The leading edge of this overturn is moving faster than the trailing edge by about 0.10 m s^{-1} . If this is the overturning velocity, U' , a very rough scaling of the energy dissipation rate for this feature is $\epsilon \approx U'^2/T$, where $T = 3000 \text{ s}$ is the duration of the overturn. This gives $\langle \epsilon \rangle \approx 3 \times 10^{-6} \text{ m}^2 \text{ s}^{-3}$, close to the observed value.

The third dissipative feature occurs at 07:00 between 550 and 650 m, after the first rise of the deep isopycnals. This region is characterized by weak vertical and strong horizontal stratification. The shape of the isopycnals is very reminiscent of the hydraulic response observed in the lee of sills such as that in Knight Inlet (Farmer and Armi 1999; Klymak and Gregg 2003). There is a strongly stratified plunging flow peeling off and adjusting to the downstream condition, forming a turbulent bore-like feature. This bore carries a 75-m thick bolus of well-mixed and overturning water moving on-ridge. The plunging flow appears to strum three 50-m tall rebounds on the deeper isopycnals, again reminiscent of sill flows.

FIG. 14

c. Tidal Phase Averages

The trends in the deep data are robust from tide to tide, as demonstrated by tidal-phase averages (Fig. 15). Tidal phase is determined for the whole cruise on a 12.4-hour period and then the quantities binned by 20 minutes in tidal phase and 20 m vertically. Zero tidal phase is slack barotropic flow before it changes to on-ridge. The averages are carried out over intervals representing neap and spring tides Fig. 2.

FIG. 15

The differences in the spring and neap forcing are clear. As in the example above, the first neap tide has maximum isopycnal displacements approaching 100 m, but weak turbulence, except in the bottom 50 m. The first spring tide has larger isopycnal displacements, but the tide is more asymmetric, with the leading edge sharper than the trailing edge. This leading edge has strong turbulence, while the trailing edge has weaker. The second neap tide is very weak, with isopycnal displacements not exceeding 50 m, and almost no turbulence. The last spring tide has the strongest displacements, over 150 m, and a very pronounced phase locking of the turbulence to the tide.

The phase averaging emphasizes the deterministic link between the tide and the dissipation rate above Kaena Ridge. We attribute this strong dissipation to the very impressive strain at the leading edge of the tidal peak (Fig. 16). At the leading edge, the strain $((N^2/N_0^2)^{-1})$ is much higher than on the trailing edge. Shear, S^2 , on the other hand, is not very strong, and is in fact larger during the trough of the internal tide where there is not as much turbulence.

d. The spring-neap cycle

The spring-neap variability of ϵ for the cruise is approximately a factor of 30 near the ridge crest (Fig. 17d,e). Further up in the water column the correlation with the tide is reduced and spikes in the record are less deterministic (Fig. 17b,c). Here we quantify the correlation of the dissipation rate with the tidal forcing. We may expect, *a-priori* that the dissipation will scale with the energy put into the tide. Using lin-

ear tide generation models this is proportional to U^2 (St. Laurent and Garrett 2002; Llewellyn Smith and Young 2003).

The spring-neap variability obeys a relatively tight power law in each depth bin, though the power changes with depth (Fig. 17f–i). In the shallowest depth bin the dependence is very weak, but in the deeper bins it varies from $\epsilon \sim (U^2 + V^2)^2$ to $\epsilon \sim (U^2 + V^2)^3$. This variation is not monotonic, with the strongest dependence occurring from 550–650 m. This reflects what was seen in the individual examples, where strong breaking occurred at these depths for the strongest tides. Deeper than 450 m the dependence on tidal forcing is much stronger than indicated by a simple proportionality with linear forcing, reflecting the non-linear nature of the turbulence. In the shallow bins, however, it is weaker ($\epsilon \sim U$). The same weak dependence on tidal forcing was found offshore of the ridge in repeated surveys by a towed turbulence vehicle (Klymak et al. 2006).

4. Turbulence mechanisms

a. What triggers turbulence?

Above, we assert that the strongest dissipation values are associated with large strain, particularly during the phase of the internal tide corresponding to the rise of deep isopycnals. This holds true statistically as well. The following analysis is similar to that found in Alford and Pinkel (2000b), with similar results.

We consider shear and strain during the first spring tide period. Here, strain is defined as the inverse of the stratification anomaly:

$$St = \frac{N_0^2}{N^2}, \quad (5)$$

where N_0^2 is the cruise-mean stratification at each depth. For comparison with the shear statistic, N^2 is smoothed over 4 m. Shear is normalized by the mean stratification. The

probability distribution functions (PDFs) of strain and shear can be compared to the conditional PDFs of the same quantities when overturns are present.

The results demonstrate that strain is a much better predictor of overturns than shear at the resolved scales (Fig. 18). The PDF of shear conditionally sampled when there is an overturn is almost identical to the unconditional PDF. On the other hand, there is a strong tendency for overturns to be associated with anomalously high strains (low stratification).

FIG. 18

Regions of high strain also tend to have higher dissipation rates (Fig. 19a–b). Here we compare the average dissipation for each mean stratification by using the normalized dissipation rate:

$$K_p = 0.2 \frac{\varepsilon}{N_0^2}, \quad (6)$$

Regions of high strain have higher than average dissipation rates (Fig. 19a), but the anomaly is not as pronounced as the occurrence of overturns would indicate. Overturn events at high stratification, while rare, have stronger dissipation values associated with them. This is true using either the micro-conductivity or overturn method of estimating ε .

The mean dissipation rate as a function of shear, on the other hand, is almost exactly a constant (Fig. 19c–d). This is consistent with the probability of finding an overturn being independent of shear. It is also consistent with shear not being a predictor of dissipation strength.

FIG. 19

A possible objection is that the shear is not local to the overturns because it is being measured using four beams from a Doppler sonar. 300-m below the sonar, the beams are 350 m apart. If the advection speed past the sensors is on the order of 0.1 m s^{-1} , then 3600 s is approximately the time over which a given feature is smeared. Applying this smoothing to the strain and dissipation fields, however, yields the same statistics except for a tightening of the PDFs (not shown for brevity). This indicates that the events that are associated with dissipation last longer than an hour, plenty of time for the high-shear associated with them to have been detected by the sonar. The alternative

is that the events are triggered by shear in patches less than 350-m wide. We cannot test this, but it seems unlikely given what is known about aspect ratios in the ocean.

This analysis simply reinforces what can be seen visually in Fig. 16. The largest overturns are associated with convective breaking of the internal tidal wave. These overturns last for a long time, and are not likely associated with a shear instability. Of course, as is shown below, this is not an open-ocean wavefield, however, these findings correspond well to the previous results of Alford and Pinkel (2000b).

b. Comparison of turbulence to open-ocean parameterizations

Turbulence in the open ocean is presently parametrized using a measure of the energy level of the broadband wavefield (Henyei et al. 1986; Gregg 1989; Gregg et al. 2003). Here the most basic form of this parameterization is used, which requires measurement of the shear on ~ 10 -m scales, and the local stratification to give:

$$\varepsilon_{GH} = 1.2 \times 10^{-9} \frac{\langle S^2 \rangle^2}{\langle N^2 \rangle N_0^2} \quad (7)$$

where the factor 1.2×10^{-9} includes the latitude dependence of the parameterization (Gregg et al. 2003). $S^2 = 2 * \left(\left(\frac{\partial U}{\partial z} \right)^2 + \left(\frac{\partial V}{\partial z} \right)^2 \right)$, where the factor 2 approximately corrects for smoothing of the shear field by the Doppler sonar.¹ The averages must be carried out for a sufficiently long time to get a sampling of the statistics of the wavefield.

FIG. 20

The parametrization was calculated for 20-cast (80 minutes) averages of the fields, and then the resulting dissipation fields were averaged across each of the four time periods (Fig. 20). The shallower half of the water column shows excellent agreement between the Gregg-Henyey parameterization and the more-direct estimates of the tur-

¹We are not rigorously deriving this correction factor for our measurements here. Doing so adjusts the amplitude of the predicted dissipation rate, but not its dynamic range or depth profile. The factor of 2 is close to Gregg and Sanford (1988) for 10-m shear from a falling probe. Our sonar has 4-m resolution in the vertical, but a reduction of mean shear because of horizontal beam separation (Alford and Pinkel 2000b), so the factor of 2 is a good approximation

bulence dissipation. These profiles do not change appreciably during our deployment, usually near $0.2 \langle \varepsilon \rangle \langle N^{-2} \rangle \approx 5 \times 10^{-5} \text{ m}^2\text{s}^{-1}$, with a slight increase with depth.

The deeper half of the records are more variable, and exceed predictions of the Gregg-Henyey parametrization. The parametrization yields that $0.2 \langle \varepsilon \rangle \langle N^{-2} \rangle \approx 5 \times 10^{-5} \text{ m}^2\text{s}^{-1}$, with no apparent depth dependence, and no spring-neap cycle. The observed ε is significantly greater than predicted from the parametrization, the discrepancy increasing with depth until they diverge by almost two orders of magnitude at the bottom of the measurement domain.

5. Summary and Discussion

There appear to be two distinct mechanisms producing turbulence in our records. The first is the near-bottom convective breaking of the internal tide which:

1. is phase locked with the tide, occurring at the leading edge of the internal tide wave near the bottom. It appears to be associated with high-mode baroclinic waves of ~ 1 -km horizontal wavelength.
2. and produces turbulence whose magnitude is directly related to the that of the barotropic forcing.

The second is found in the upper water column and is more typical of turbulence dissipation in a broadband internal wave field:

1. it is predicted from the ambient shear and strain.
2. it has no readily-apparent spring-neap cycle.

a. Comparison direct dissipation observations

As part of HOME, a comprehensive survey of turbulence dissipation was made on the Ridge using "microstructure" sensors. The average dissipation profiles are presented in Klymak et al. (2006). The data in that study were divided into two classes,

those from stations of water depth shallower than 500 m and those from deeper stations (See also Carter et al. 2006). The composite used from the deeper stations is shown in Fig. 20, and our measurements agree with it quite well. The composite was an idealization of the mean profile (last panel, Fig. 20, light gray).

The present data differ most strongly from the Klymak et al. (2006) data during spring tides. That study did not attempt to differentiate between spring and neap tides, and it appears likely that it underestimated the spring-tide influence near the seafloor. Klymak et al. (2006) estimate the total dissipation on top of the ridge to be 0.4 kW m^{-1} using the structure in Fig. 20. Assuming that we have underestimated the bottom 600 m by a factor of ten during spring tides (approximately half the time), then we get a number closer to 1 kW m^{-1} , yielding an increase over the whole cross-section from 1.4 kW m^{-1} to 2 kW m^{-1} . Since the ridge-wide dissipation estimate in Klymak et al. (2006) was scaled to this cross-ridge section, the total number could be underestimated by 40%, and may rise from 2.5 GW to 4.3 GW. This is still within the error bounds given in the previous study, but on the high end. In terms of a “radiation efficiency” (St. Laurent and Garrett 2002), about $q = 0.2$ of the 20 GW of barotropic energy may go into local turbulence.

b. Comparison with mooring measurements

Overtuns have been detected at two moorings (so far) near the Hawaiian Ridge, one on the north flank (Levine and Boyd 2006, “BigBoy”, Fig. 1) and one on the south flank (Aucan et al. 2006, “DS”, Fig. 1). Both studies are consistent with the present findings.

- tide phase-locked turbulence dissipation events near the sea-floor,
- strong spring-neap cycles to the dissipation.

The non-linear tidal waveform assumes a different structure on the slopes relative to the summit observations made from *R/P FLIP*. At the north site, the up-slope flow

of dense water has strong stratification, and weak mixing, except very near the bottom, where a shear-driven regime is found at peak upslope tide (Levine and Boyd 2006). The strongest turbulence is found when the near-bottom flow is off-slope, making the stratification weaker.

This downslope flow mechanism appears active at the south site. The strongest turbulence, however, happens during times of somewhat stronger mean stratification when the flow reverses from downslope to upslope (Aucan et al. 2006). When the events occur, there appear to be sharp fronts when the isopycnals are rapidly rising.

Our data are consistent with both sets of observations, particularly during spring tides. The strongest dissipation values are observed when the tidally-modulated stratification is the lowest (Fig. 16), with a patch near 500 m during the drop of the internal tide, and the strongest dissipation near 700 m during the sharp rise of the internal tide. However, our tidal structure is different than Levine and Boyd (2006), in that the most rapid change of isopycnal displacement is while they are rising, rather than dropping.

The common element is that the near-bottom dissipation events are tied in a relatively regular fashion to the non-linear structure of the internal tide. Levine and Boyd (2006) attempt a simple estimate of the first-order non-linearity along the slope by assuming that the observed velocity is linear and integrating to estimate the isopycnal displacements. This does not explain why the velocity has the phase and amplitude that is observed, so the predictive power of this model is somewhat limited. However, this weakly nonlinear calculation does a good job of predicting the non-linearity of the density field near their mooring.

We emphasize, however, that our measurements are not made directly at the sea-floor, but rather 300 m aloft. They are also made over a nearly flat bottom, and furthermore, we see distinct patches of turbulence that are isolated vertically from the bottom of our measurement domain. Therefore, we feel that we are looking at a non-linear internal wave phenomenon, rather than a bottom-drag induced convective instability as proposed by Slinn and Levine (2003) and observed in the bottom Ekman layer on the Oregon shelf by Moum et al. (2004) and in a lake by Lorke et al. (2005).

c. Dissipation mechanism shallower than 400 m

The mixing above 400 m depth varies only weakly with the tidal forcing on a fortnightly scale, and not at all on a daily scale. The dissipation also agrees very well with the Gregg-Henyey model. The model assumes that energy put into the broadband wavefield at large scales undergoes a cascade to small scales. The rate of this cascade is believed to be proportional to the square of the energy in the broadband wavefield. It appears that at this site, the shallower half of the water column is being forced in this manner.

If, as seems reasonable, the dominant forcing of the wavefield at these depths is the tide, then the dissipation is buffered from the forcing because of the lack of a strong daily and spring-neap cycle. This is consistent with the Gregg-Henyey model, so long as the time it takes for the cascade from the tide to the dissipation is on the order of the spring-neap period (≈ 14 days). Klymak et al. (2006) found a similar dependence in towed body data ($\epsilon \sim U$), and demonstrate that this could be arrived at if the tidal signal was smoothed by approximately 5 days. A similar time scale has been postulated for parametric subharmonic instability of internal waves (MacKinnon and Winters 2005), lending indirect evidence to the importance of this wave-wave interaction to the direct evidence presented by Carter and Gregg (2006).

d. Implications of near-seafloor breaking

The direct breaking of the tide at the Hawaiian Ridge contrasts distinctly from typical open ocean tidal dissipation mechanisms. It is, however, quite similar to the mechanisms seen in fjords such as Knight Inlet (Freeland and Farmer 1980), and tested by Klymak and Gregg (2004). In the latter paper, direct dissipation of internal waves was thought to account for 10% of the total dissipation near the sill. Sidewall effects were estimated to be a bigger local loss, though that is not a factor in Hawaii.

The origin of the non-linearity and breaking was difficult to observe with at-sea measurements such as fixed moorings and *R/P FLIP*. To get a better idea of the origins,

Legg and Klymak (2007) ran a two-dimensional fully non-hydrostatic model of the response of the ridge to a tidal forcing (Fig. 21). These simulations show that the response observed at *R/P FLIP* has its origins in a internal hydraulic response at the break in the ridge topography approximately 2 km south. In the model the non-linear response forms during off-ridge flow and is subsequently swept past *R/P FLIP* when the flow reverses. Preliminary analysis of these results is given in more detail in Legg and Klymak (2007), and further model-data comparisons are the subject of current research.

FIG. 21

We do not yet have a turbulence parametrization for this near-bottom dissipation. The numerical modeling indicates that the turbulence mechanism at the Hawaiian Ridge is similar to hydraulic phenomenon observed in fjords (Legg and Klymak 2007). However, instead of acting on low-modes, the hydraulics at Hawaii appear to only act on high modes that have vertical wavelengths on the order of 400 m. This is in qualitative agreement with the present observations where the breaking occurs on waves of vertical wavelength much less than the total water depth. If the suspicion that the direct turbulence mechanism is related to super-criticality and hydraulics in the flow is correct, it may serve to estimate the energy generated in high modes via a linear mechanism such as that proposed by St. Laurent and Garrett (2002), and assume that all breaks locally. The high power of turbulence dissipation with forcing may be a function of lower modes becoming super critical as tidal forcing increases.

Acknowledgements. We would like to thank the Captain and crew of *R/P FLIP* for their efforts in deploying and operating the platform. The expertise of the Ocean Physics Group made this paper possible: E. Slater, M. Goldin, L. Green, M. Bui, A. Aja, J. Pompa, T. Huguen, and J. Crockett. Discussions and modeling with S. Legg were very valuable, as were input from the members of the HOME group and our guests at various analysis meetings. This work was funded by the National Science Foundation as a component of the Hawaii Ocean Mixing Program. Added support for FLIP was provided by the Office of Naval Research.

REFERENCES

- Alford, M., and R. Pinkel, 2000a: Patterns of turbulent and double-diffusive phenomena: Observations from a rapid-profiling microconductivity probe. *J. Phys. Oceanogr.*, **30**, 833–854.
- Alford, M. H., and R. Pinkel, 2000b: Observations of overturning in the thermocline: The context of ocean mixing. *J. Phys. Oceanogr.*, **30**, 805–832.
- Aucan, J., M. A. Merrifield, D. S. Luther, and P. Flament, 2006: Tidal mixing events on the deep flanks of Kaena Ridge, Hawaii. *J. Phys. Oceanogr.*, **36**, 1202–1219.
- Baines, P. G., 1995: *Topographic Effects in Stratified Flows*. Cambridge Univ. Press, New York.
- Batchelor, G. K., 1959: Small-scale variation of convected quantities like temperature in turbulent fluid. *J. Fluid Mech.*, **5**, 113–139.
- Carter, G., M. Gregg, and M. Merrifield, 2006: Flow and mixing around a small seamount on Kaena Ridge. *J. Phys. Oceanogr.*, **36**, 1036–1052.
- Carter, G. S., and M. C. Gregg, 2006: Persistent near-diurnal internal waves observed above a site of m_2 barotropic-to-baroclinic conversion. *J. Phys. Oceanogr.*, **36**, 1136–1147.
- Dillon, T. M., 1982: Vertical overturns: A comparison of Thorpe and Ozmidov length scales. *J. Geophys. Res.*, **87**, 9601–9613.
- Egbert, G. D., and S. Y. Erofeeva, 2002: Efficient inverse modeling of barotropic ocean tides. *J. Atmos. Ocean. Tech.*, **19**, 183–204.
- Farmer, D. M., and L. Armi, 1999: Stratified flow over topography: The role of small scale entrainment and mixing in flow establishment. *Proc. R. Soc. London, Ser. A*, **455**, 3221–3258.
- Freeland, H. J., and D. M. Farmer, 1980: Circulation and energetics of a deep, strongly stratified inlet. *Can. J. Fish. Aquat. Sci.*, **37**, 1398–1410.
- Garrett, C., and E. Kunze, 2007: Internal tide generation in the deep ocean. *Ann. Rev. Fluid Mech.*, 57–87.

- Gregg, M. C., 1989: Scaling turbulent dissipation in the thermocline. *J. Geophys. Res.*, **94**, 9686–9698.
- Gregg, M. C., and T. B. Sanford, 1988: The dependence of turbulent dissipation on stratification in a diffusively stable thermocline. *J. Geophys. Res.*, **93**, 12381–12392.
- Gregg, M. C., T. B. Sanford, and D. P. Winkel, 2003: Reduced mixing from the breaking of internal waves in equatorial waters. *Nature*, **422**, 513–515.
- Henye, F. S., J. Wright, and S. M. Flatté, 1986: Energy and action flow through the internal wave field. *J. Geophys. Res.*, **91**, 8487–8495.
- Hibiya, T., and M. Nagasawa, 2004: Latitudinal dependence of diapycnal diffusivity in the thermocline estimated using a finescale parameterization. *Geophys. Res. Lett.*, **31**, L01301, doi:10.1029/2003GL017998.
- Inall, M. E., T. Rippeth, C. Griffiths, and P. Wiles, 2005: Evolution and distribution of the production and dissipation within stratified flow over topography. *Geophys. Res. Lett.*, **32**, L08607, doi:10.1029/2004GL022289.
- Johnston, T. S., and M. A. Merrifield, 2003: Internal tide scattering at seamounts, ridges, and islands. *J. Geophys. Res.*, **108**, 3180, doi:10.1029/2002JC01528.
- Klymak, J. M., and M. C. Gregg, 2003: The role of upstream waves and a downstream density-pool in the growth of lee-waves: stratified flow over the Knight Inlet sill. *J. Phys. Oceanogr.*, **33**, 1446–1461.
- 2004: Tidally generated turbulence over the Knight Inlet sill. *J. Phys. Oceanogr.*, **34**, 1135–1151.
- Klymak, J. M., and J. N. Moum, 2007: Interpreting spectra of horizontal temperature gradients in the ocean: Part II - turbulence, in press, *J. Phys. Oceanogr.*
- Klymak, J. M., J. N. Moum, J. D. Nash, E. Kunze, J. B. Girton, G. S. Carter, C. M. Lee, T. B. Sanford, and M. C. Gregg, 2006: An estimate of tidal energy lost to turbulence at the Hawaiian Ridge. *J. Phys. Oceanogr.*, **36**, 1148–1164.
- Lee, C. M., E. Kunze, T. B. Sanford, J. D. Nash, M. A. Merrifield, and P. E. Holloway, 2006: Internal tides and turbulence along the 3000-m isobath of the Hawaiian

- Ridge with model comparisons, in press *J. Phys. Oceanogr.*
- Legg, S., and A. Adcroft, 2003: Internal wave breaking at concave and convex continental sloped. *J. Phys. Oceanogr.*, **33**, 2224–2246.
- Legg, S., and J. M. Klymak, 2007: Internal hydraulic jumps and overturning generated by tidal flow over a steep ridge, in review, *J. Phys. Ocean.*
- Levine, M. D., and T. J. Boyd, 2006: Tidally-forced internal waves and overturns observed on a slope: results from the HOME survey component. *J. Phys. Oceanogr.*, **36**, 1184–1201.
- Llewellyn Smith, S. G., and W. R. Young, 2003: Tidal conversion at a very steep ridge. *J. Fluid Mech.*, **495**, 175–191.
- Lorke, A., F. Peeters, and A. Wüest, 2005: Shear-induced convective mixing in bottom boundary layers on a slopes. *Limnol. Oceanogr.*, **50**, 1612–1619.
- MacKinnon, J. A., and K. B. Winters, 2005: Reconsidering a disqualified candidate for the energy balance of oceanic internal waves, submitted *J. Phys. Oceanogr.*
- Martin, J. P., D. L. Rudnick, and R. Pinkel, 2006: Spatially broad observations of internal waves in the upper ocean at the Hawaiian Ridge, in press, *J. Phys. Oceanogr.*
- Merrifield, M. A., and P. E. Holloway, 2002: Model estimate of m_2 internal tide energetics at the Hawaiian Ridge. *J. Geophys. Res.*, **107**, 10.1029/2001JC000996.
- Moum, J. N., 1996a: Efficiency of mixing in the main thermocline. *J. Geophys. Res.*, **101**, 12059–12069.
- 1996b: Energy-containing scales of turbulence in the ocean thermocline. *J. Geophys. Res.*, **101**, 14095–14109.
- Moum, J. N., A. Perlin, J. Klymak, M. Levine, T. Boyd, and M. Kosro, 2004: Convectively-driven mixing in the bottom boundary layer. *J. Phys. Oceanogr.*, **34**, 2189–2202.
- Nash, J. D., E. Kunze, C. M. Lee, and T. B. Sanford, 2006: Structure of the baroclinic tide generated at Kaena Ridge, Hawaii. *J. Phys. Oceanogr.*, **36**, 1123–1135.
- Nash, J. D., E. Kunze, J. M. Toole, and R. W. Schmitt, 2004: Internal tide reflection and turbulent mixing on the Continental Slope. *J. Phys. Oceanogr.*, 1117–1134.

- Osborn, T. R., 1980: Estimates of the local rate of vertical diffusion from dissipation measurements. *J. Phys. Oceanogr.*, **10**, 83–89.
- Pinkel, R., 2006: Advection, phase distortion, and the frequency spectrum of fine-scale fields in the sea, submitted to the *J. Phys. Oceanogr.*
- Polzin, K., 2004: Idealized solutions for the energy balance of the finescale internal wave field. *J. Phys. Oceanogr.*, **34**, 231–246.
- Rainville, L., and R. Pinkel, 2006: Observations of the propagation and nonlinear interaction of the internal tide generated at the Hawaiian Ridge. *J. Phys. Oceanogr.*, **36**, 1104–1122.
- Rudnick, D. L., T. J. Boyd, R. E. Brainard, G. S. Carter, G. D. Egbert, M. C. Gregg, P. E. Holloway, J. M. Klymak, E. Kunze, C. M. Lee, M. D. Levine, D. S. Luther, J. P. Martin, M. A. Merrifield, J. N. Moum, J. D. Nash, R. Pinkel, L. Rainville, and T. B. Sanford, 2003: From tides to mixing along the Hawaiian Ridge. *Science*, **301**, 355–357.
- Slinn, D. N., and M. D. Levine, 2003: Modeling internal tides and mixing over ocean ridges. *Near-Boundary Processes and Their Parameterization Proceedings of the 13th 'Aha Huliko'a Hawaiian Winter Workshop*, P. Müller and C. Garrett, eds.
- St. Laurent, L., and C. Garrett, 2002: The role of internal tides in mixing the deep ocean. *J. Phys. Oceanogr.*, **32**, 2882–2899.
- St. Laurent, L. C., J. M. Toole, and R. W. Schmitt, 2001: Buoyancy forcing by turbulence above rough topography in the abyssal Brazil Basin. *J. Phys. Oceanogr.*, **31**, 3476–3495.
- Thorpe, S. A., 1977: Turbulence and mixing in a Scottish loch. *Phil. Trans. Roy. Soc. London, Ser. A*, **286**, 125–181.

Draft: Revision : 1.4 Date : 2007/04/11 21 : 38 : 45 April 17, 2007

Generated with ametsocjmk.cls.

Written by J. M. Klymak

mailto:jklymak@uvic.ca

<http://web.uvic.ca/jklymak/WorkTools.html>

Figure Captions

FIG. 1. *R/P FLIP* was moored in 1100 m of water over Kaena Ridge at $21^{\circ}40.78'$ N, $158^{\circ}37.77'$ W. Also shown are two moorings from the same field program, where large near-bottom overturns have also been observed (see text).

FIG. 2. Predicted amplitude of tidal velocity from the OTIS model (Egbert and Erofeeva 2002) at the location of *R/P FLIP*. Times discussed in the paper are indicated with the solid lines, alternating between neap and spring.

FIG. 3. a) Profiles of potential density (black), density-scaled temperature ($\alpha\rho T$, shaded line), and density-scaled salinity ($\beta\rho S$, dashed-shaded line). b) parcel displacement, density (L_{ρ} black) and temperature (L_{θ} shaded). c) stratification from sorted profile (thin black) and for the overturns (thick black for density, thick shaded for temperature). d) Turbulence estimate; thin line is from micro-conductivity probe (see below), solid lines are from density (black) and temperature (shaded).

FIG. 4. Example conductivity-derivative spectra compared to SeaBird 9/11 sensor. The correction to the microconductivity sensor is both a correction for a pre-emphasis circuit, and an *in-situ* gain correction.

FIG. 5. Mean profiles (left panel) and ratio (right panel) of the gradients of temperature (black) and salinity (gray), measured from the macro-conductivity cell. The

temperature gradient dominates the salinity gradient for the whole water column, not dropping below a factor of five difference.

FIG. 6. Two example microconductivity fits from turbulent and quiet portions of a drop. The fit is made between 4 and 9 cyc m^{-1} (thick shaded lines).

FIG. 7. Comparison between the two dissipation estimates made in this paper. a) and c) are probability-density functions (PDFs) of ϵ_ρ for each bin of ϵ_χ . Both signals have been smoothed and decimated by 10 m to remove variance within individual overturns. The black band along the bottom is for data with no overturn estimate so $\epsilon_\rho = 10^{-11} \text{ m}^2 \text{ s}^{-3}$. The mean value of ϵ_ρ is shown as a function of ϵ_χ . a) is for depths 50–100 m and c) is for 420–570 m. b) and d) are corresponding total PDFs for both estimates; the mean of each distribution is indicated with a vertical line; note the means are almost identical in d).

FIG. 8. Distribution of the Ozmidov scales in shallow (60–110 m) and deep (470–570 m) calculated from the microconductivity estimate of ϵ_χ . Dashed line is 2.2-m resolution of the density measurements, so only dissipation events $L_O > 2.2$ m would be detectable by the overturn method. The percentage of the water with $L_O > 2.2$ m is compared the percentage with overturns in the legend.

FIG. 9. Effect of smoothing the density data on mean profiles of ϵ_ρ compared to profiles of ϵ_χ . Data is from the first spring tide. Note that in the averaged profiles

presented below, this time period is the one with the worst agreement between the two methods.

FIG. 10. A three tidal cycle example from neap tide early in the cruise. a) is cross-ridge barotropic velocity prediction from OTIS tidal model. b) cross-ridge velocity, smoothed 20 m vertically, and 16 minutes in time. c) ϵ_χ , d) ϵ_ρ , both smoothed logarithmically by 15 m vertically and 3 casts (12 minutes) in time (for presentation purposes). Density is contoured in (a) using the mean density from every 50 m of the mean density profile, and in (c) and (d) for every 100 m. Each panel shows approximately 540 evenly-spaced casts.

FIG. 11. Average dissipation profiles from the three time periods in Fig. 10 (neap tide), Fig. 12 (spring tide), and Fig. 13 (second spring tide). Panels (e) and (f) are only plotted from 400–800 m.

FIG. 12. As Fig. 10, except during a stronger flood tide.

FIG. 13. As Fig. 10, for the second spring tide; note that only bottom 400 m of the water column is plotted.

FIG. 14. Detail of a representative on-ridge tide (6 Oct, the day after the last cycle in Fig. 13). Contours are potential-density surfaces that are 25 m apart in the mean profile. Upper panel is the barotropic cross-ridge velocity predicted from OTIS. Second panel is ϵ_ρ , third panel is temperature, and the last panel is on-ridge velocity.

FIG. 15. Tidal phase-averages of cross-ridge velocity and turbulence dissipation from potential-density overturns (potential-density contours overlain). $t = 0$ is for slack barotropic flow before it changes to on-ridge. Four time periods are shown, two neaps and two spring tides. Dissipation is averaged arithmetically, not logarithmically, and the color scale for the dissipation is correspondingly higher.

FIG. 16. Tidal phase-averaging for the second spring tide ($t = 0$ is slack barotropic flow before the on-ridge phase). a) stratification anomaly, b) shear anomaly, and c) diffusivity (dissipation from potential-density overturns scaled by stratification). The dissipation varies by almost two orders of magnitude as the phase changes. The strain is very large where the turbulence is the highest.

FIG. 17. a) Square of the predicted tidal velocity (thin), and smoothed by 4-tidal periods (thick). b) Mean dissipation (ϵ_p) between 250-350 m, smoothed by four tidal periods (thick), and a quarter tidal period (thin). c)–e) 100-m bins going down in depth. f)–i) are the smoothed dissipation versus the smoothed tidal velocities (slightly oversampled at 2 tidal periods). The dissipation is fit as a power law to the tidal amplitude squared.

FIG. 18. a) PDF of strain (solid), and strain where there are overturns (dashed). b) Fraction of water column overturning in each strain bin. Dashed line is total fraction overturning in the water column. c) and d) same, except for shear. Data is from 450-750 m, during the first spring tide.

FIG. 19. From the first spring tide: a) mean dissipation ($K_p = 0.2\epsilon N_0^{-2}$) as a function of strain, using both ϵ_p (black) and ϵ_χ (red) b) CDF of K_p (black and red) and strain (dashed). c) and d) as (a) and (b), for shear.

FIG. 20. Average vertical profiles of turbulence dissipation, normalized by mean stratification (to make a diapycnal diffusivity) for the four time periods. Thick black line is the estimate from the microconductivity probe; thin shaded line from density overturns; thick shaded line from Gregg-Henyey parameterization (equation (7)). There was no microconductivity from the upper CTD for the second two time periods. The dashed line is the composite dissipation profile from direct turbulence measurements made in deep water atop the ridge (Klymak et al. 2006). The light-shaded band in the last panel is the actual average profile from (Klymak et al. 2006). (Fig. 2),

FIG. 21. Strain fields in a two-dimensional numerical simulation of barotropic flow over the ridge (Legg and Klymak 2007) for a) slack tide and b) after 3 h of on-ridge flow. The high-strain at 600 m, and deeper than 750 m is similar to that observed at FLIP. It originates near the ridge break (a) and propagates on-ridge as the tide switches from off-ridge to on-ridge (b).

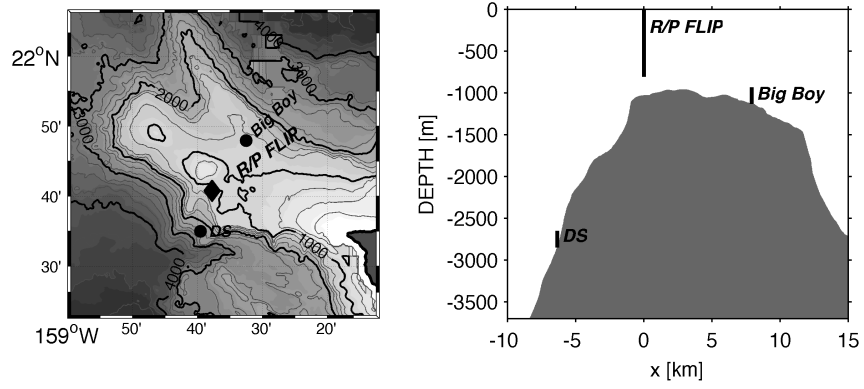


FIG. 1. *R/P FLIP* was moored in 1100 m of water over Kaena Ridge at $21^{\circ}40.78'$ N, $158^{\circ}37.77'$ W. Also shown are two moorings from the same field program, where large near-bottom overturns have also been observed (see text).

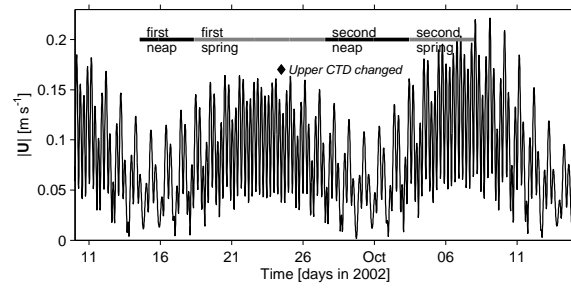


FIG. 2. Predicted amplitude of tidal velocity from the OTIS model (Egbert and Erofeeva 2002) at the location of *R/P FLIP*. Times discussed in the paper are indicated with the solid lines, alternating between neap and spring.

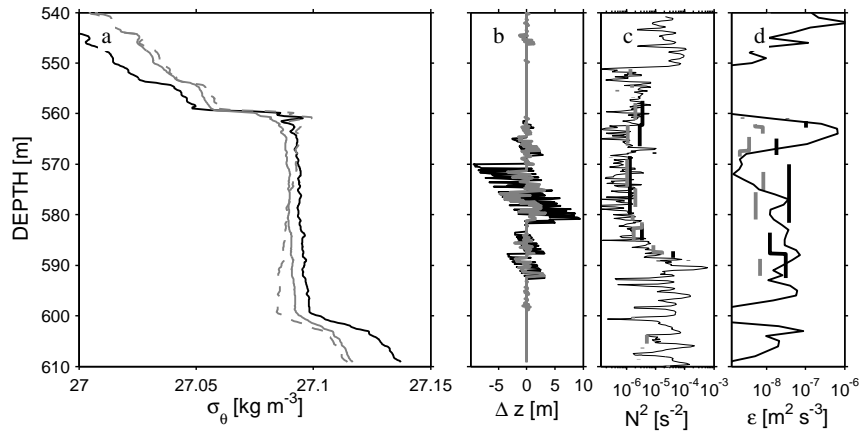


FIG. 3. a) Profiles of potential density (black), density-scaled temperature ($\alpha\rho T$, shaded line), and density-scaled salinity ($\beta\rho S$, dashed-shaded line). b) parcel displacement, density (L_ρ black) and temperature (L_θ shaded). c) stratification from sorted profile (thin black) and for the overturns (thick black for density, thick shaded for temperature). d) Turbulence estimate; thin line is from micro-conductivity probe (see below), solid lines are from density (black) and temperature (shaded).

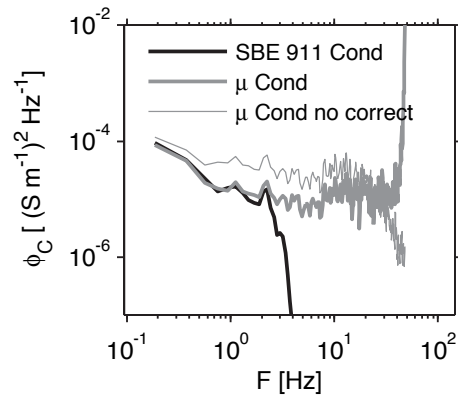


FIG. 4. Example conductivity-derivative spectra compared to SeaBird 9/11 sensor. The correction to the microconductivity sensor is both a correction for a pre-emphasis circuit, and an *in-situ* gain correction.

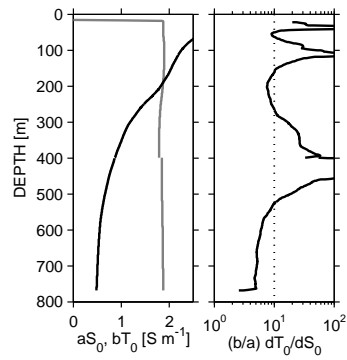


FIG. 5. Mean profiles (left panel) and ratio (right panel) of the gradients of temperature (black) and salinity (gray), measured from the macro-conductivity cell. The temperature gradient dominates the salinity gradient for the whole water column, not dropping below a factor of five difference.

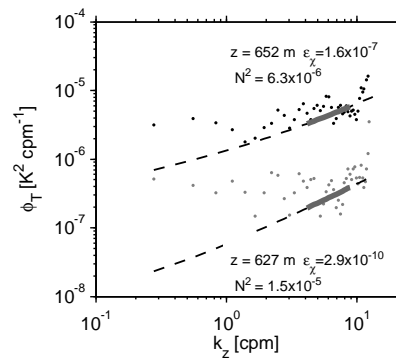


FIG. 6. Two example microconductivity fits from turbulent and quiet portions of a drop. The fit is made between 4 and 9 cyc m^{-1} (thick shaded lines).

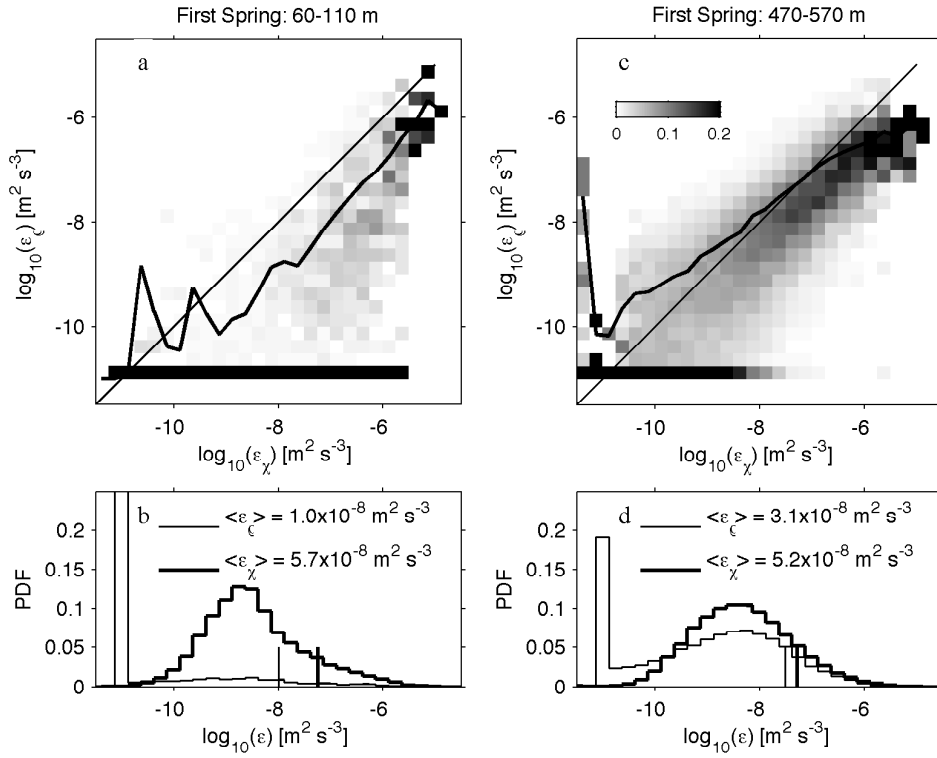


FIG. 7. Comparison between the two dissipation estimates made in this paper. a) and c) are probability-density functions (PDFs) of ϵ_ρ for each bin of ϵ_χ . Both signals have been smoothed and decimated by 10 m to remove variance within individual overturns. The black band along the bottom is for data with no overturn estimate so $\epsilon_\rho = 10^{-11} \text{ m}^2 \text{ s}^{-3}$. The mean value of ϵ_ρ is shown as a function of ϵ_χ . a) is for depths 50–100 m and c) is for 420–570m. b) and d) are corresponding total PDFs for both estimates; the mean of each distribution is indicated with a vertical line; note the means are almost identical in d).

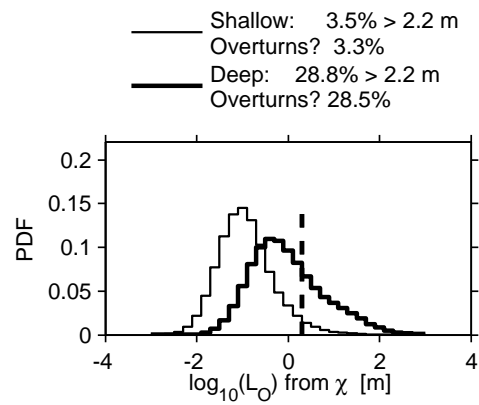


FIG. 8. Distribution of the Ozmidov scales in shallow (60–110 m) and deep (470–570 m) calculated from the microconductivity estimate of ε_χ . Dashed line is 2.2-m resolution of the density measurements, so only dissipation events $L_O > 2.2$ m would be detectable by the overturn method. The percentage of the water with $L_O > 2.2$ m is compared the percentage with overturns in the legend.

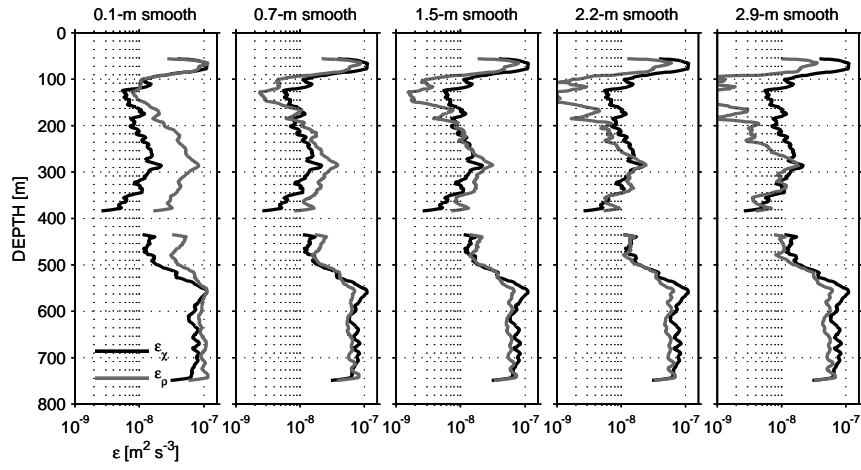


FIG. 9. Effect of smoothing the density data on mean profiles of ϵ_ρ compared to profiles of ϵ_χ . Data is from the first spring tide. Note that in the averaged profiles presented below, this time period is the one with the worst agreement between the two methods.

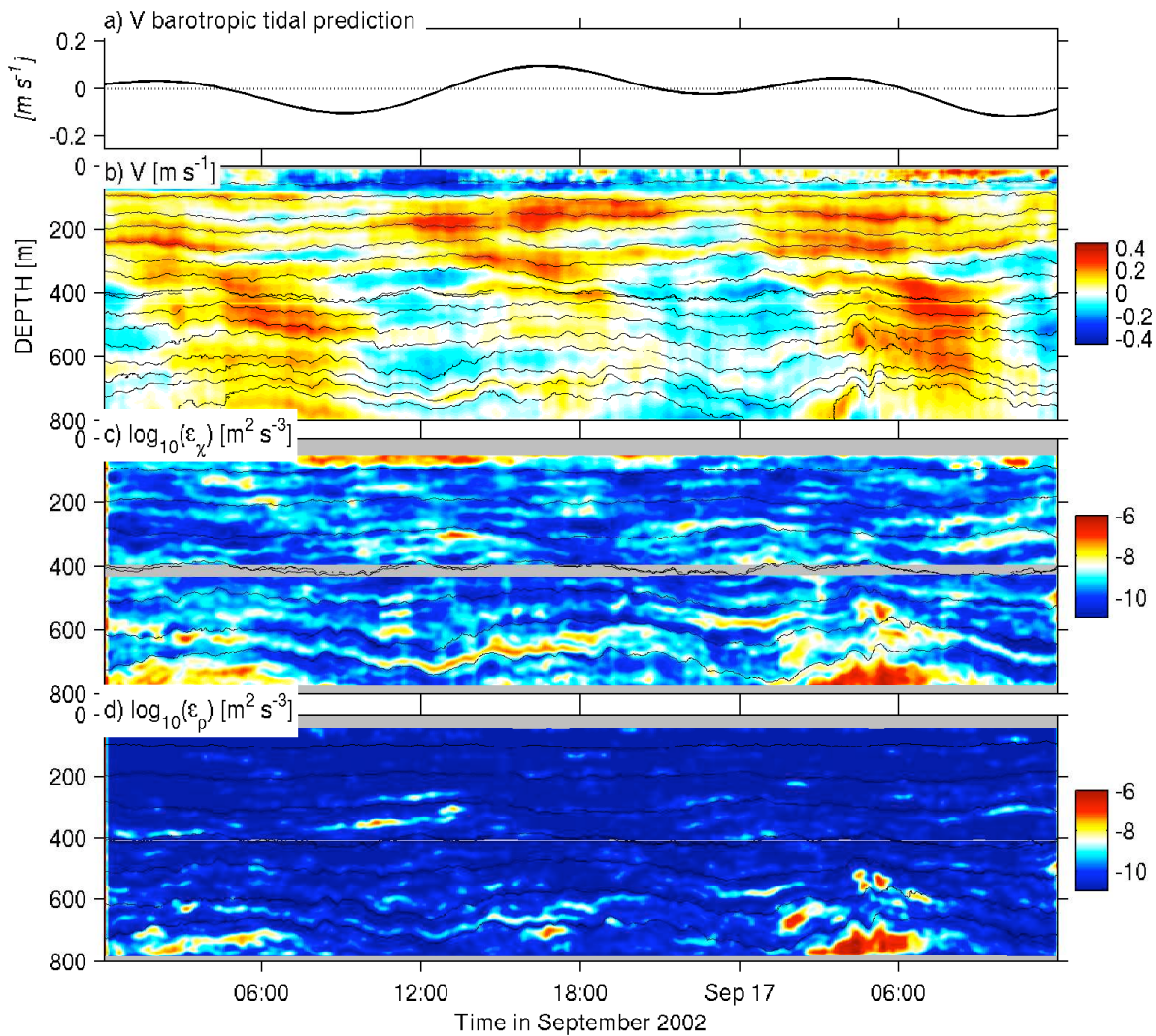


FIG. 10. A three tidal cycle example from neap tide early in the cruise. a) is cross-ridge barotropic velocity prediction from OTIS tidal model. b) cross-ridge velocity, smoothed 20 m vertically, and 16 minutes in time. c) ϵ_{χ} , d) ϵ_{ρ} , both smoothed logarithmically by 15 m vertically and 3 casts (12 minutes) in time (for presentation purposes). Density is contoured in (a) using the mean density from every 50 m of the mean density profile, and in (c) and (d) for every 100 m. Each panel shows approximately 540 evenly-spaced casts.

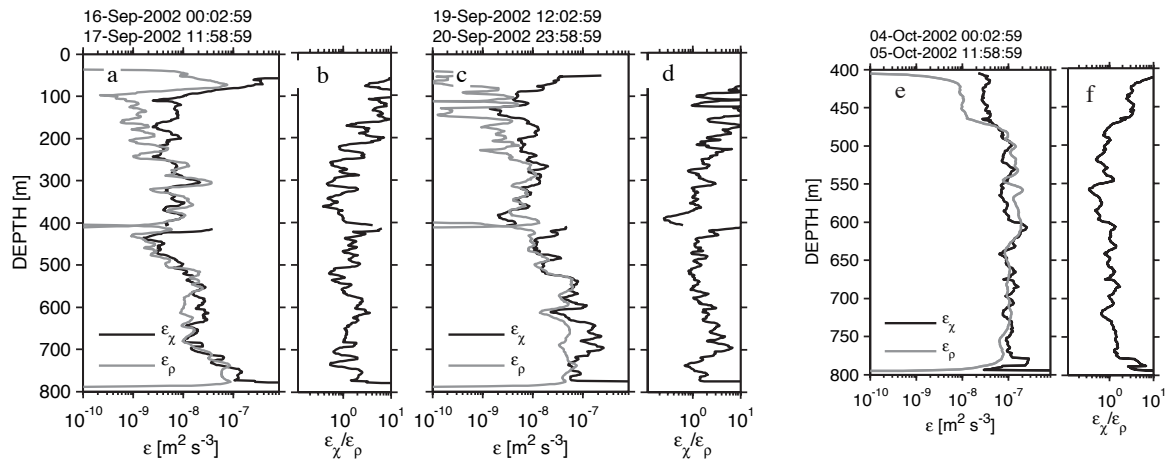


FIG. 11. Average dissipation profiles from the three time periods in Fig. 10 (neap tide), Fig. 12 (spring tide), and Fig. 13 (second spring tide). Panels (e) and (f) are only plotted from 400–800 m.

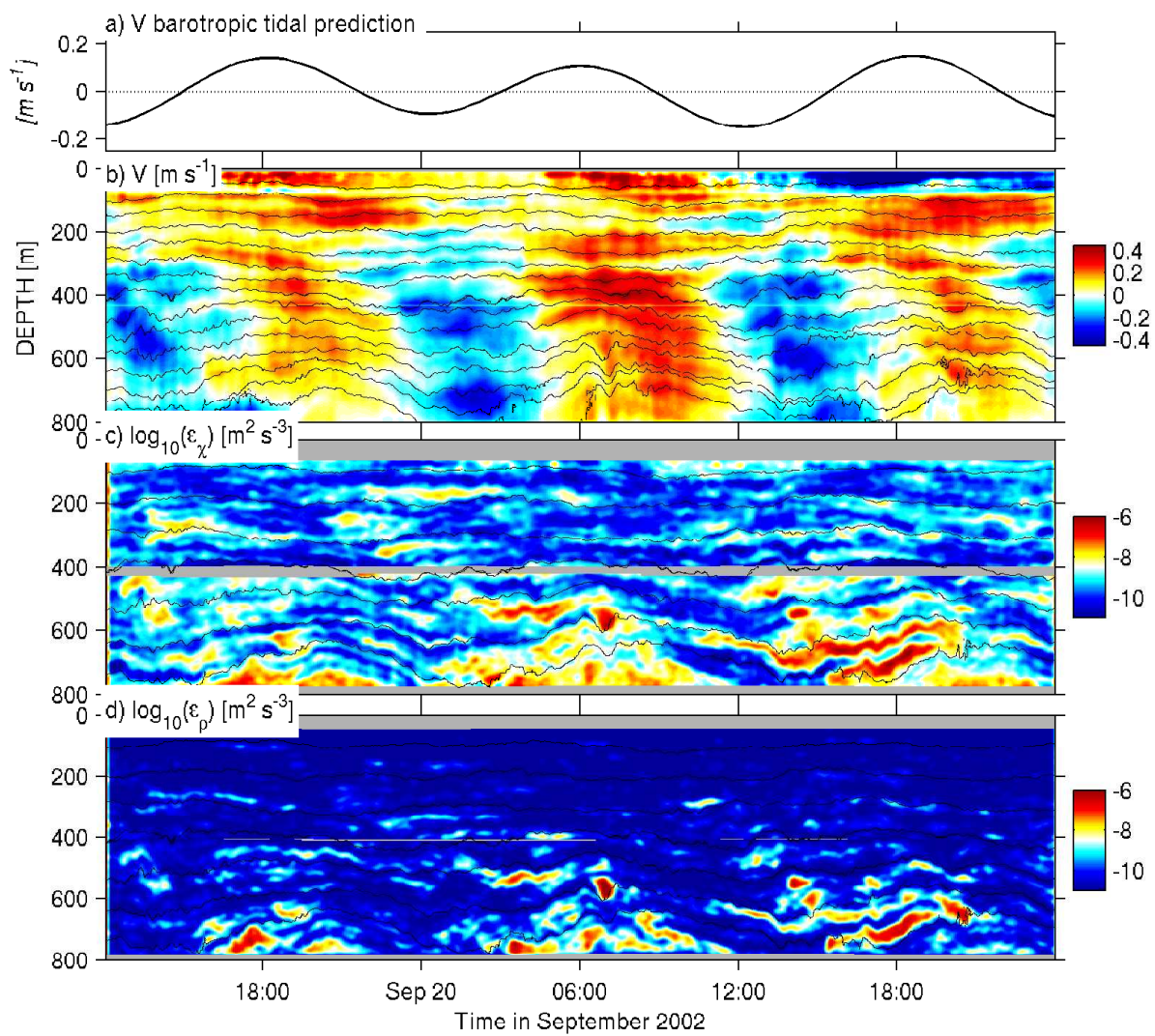


FIG. 12. As Fig. 10, except during a stronger flood tide.

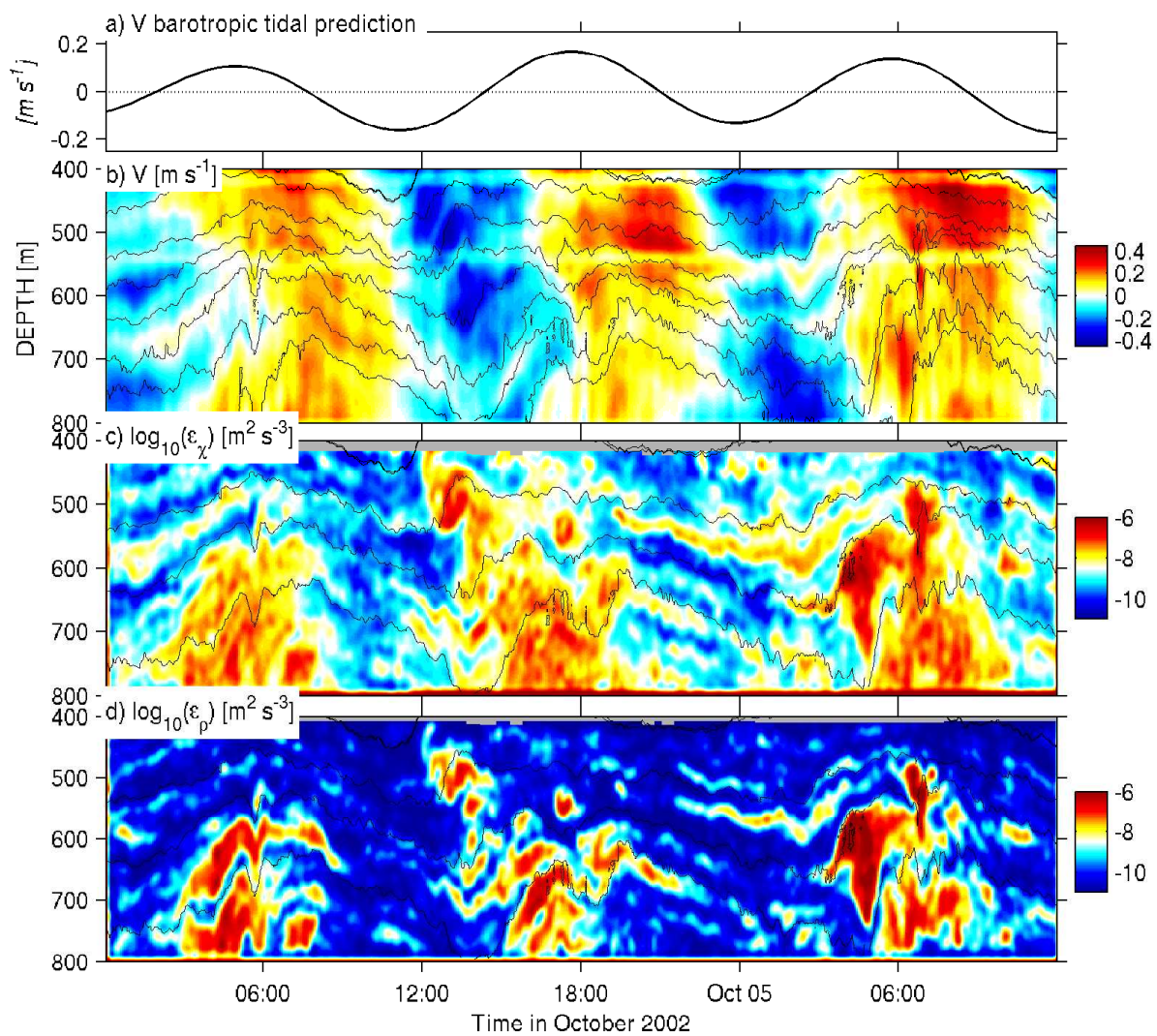


FIG. 13. As Fig. 10, for the second spring tide; note that only bottom 400 m of the water column is plotted.

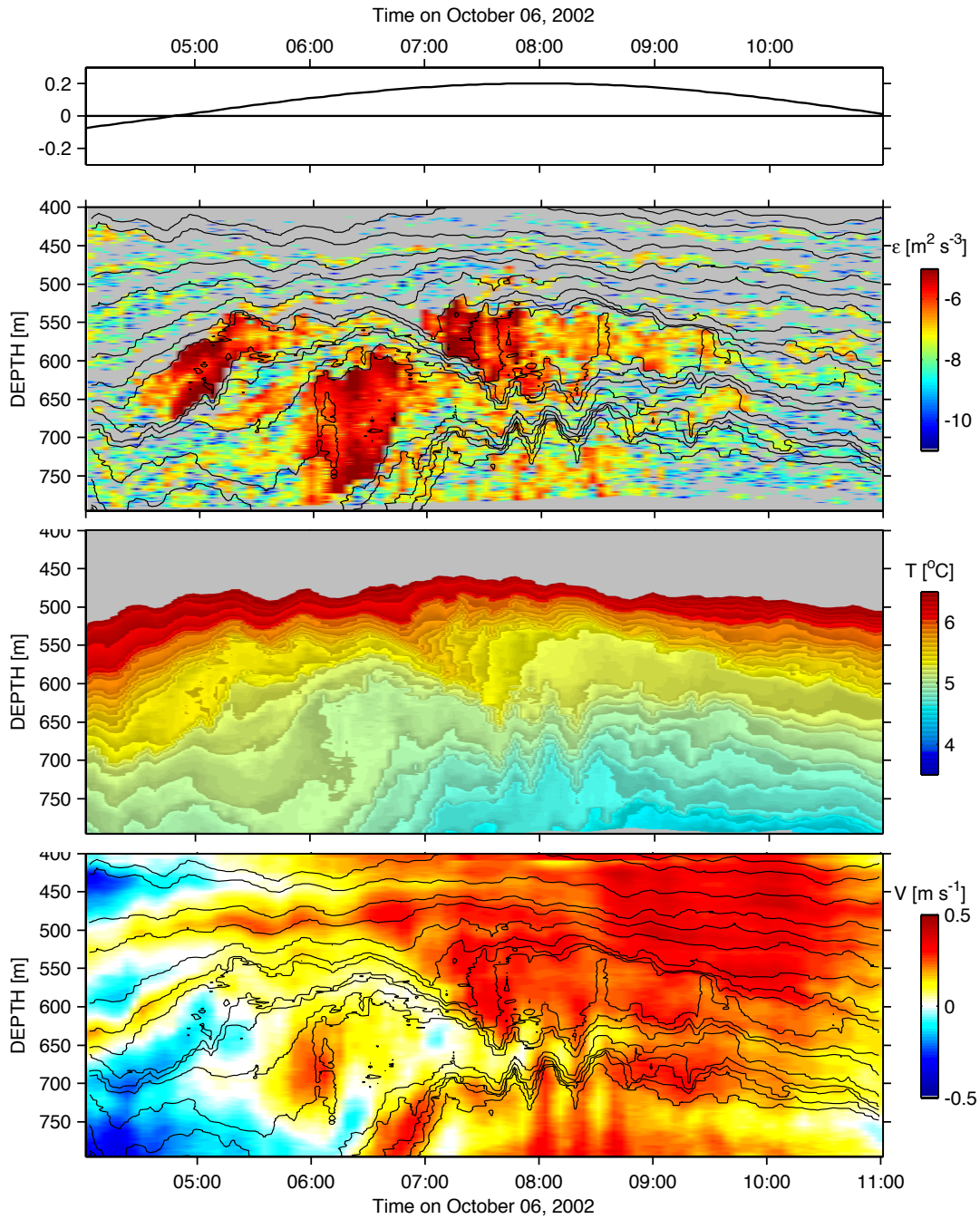


FIG. 14. Detail of a representative on-ridge tide (6 Oct, the day after the last cycle in Fig. 13). Contours are potential-density surfaces that are 25 m apart in the mean profile. Upper panel is the barotropic cross-ridge velocity predicted from OTIS. Second panel is ϵ_{ρ} , third panel is temperature, and the last panel is on-ridge velocity.

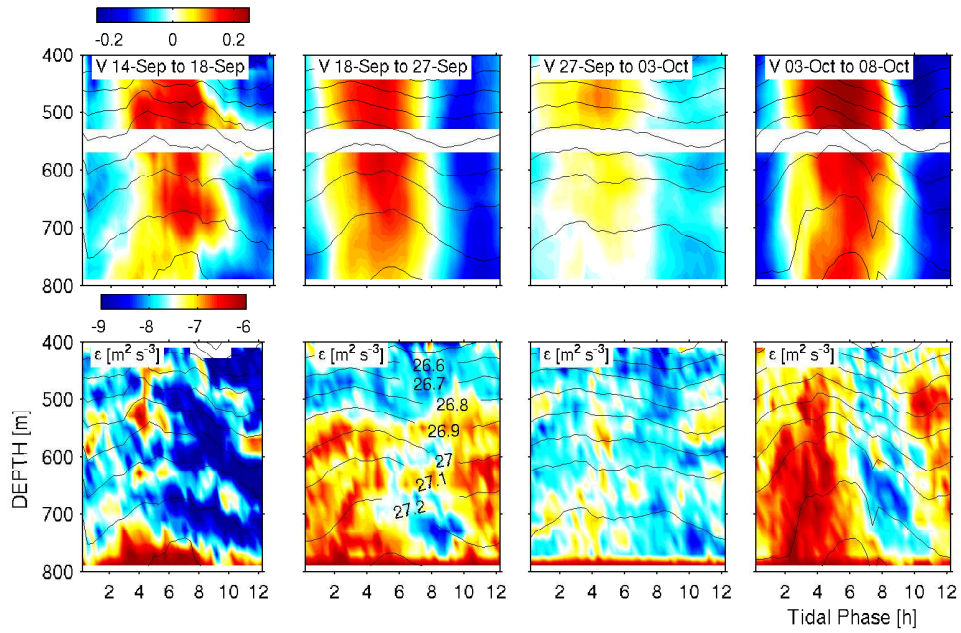


FIG. 15. Tidal phase-averages of cross-ridge velocity and turbulence dissipation from potential-density overturns (potential-density contours overlain). $t = 0$ is for slack barotropic flow before it changes to on-ridge. Four time periods are shown, two neaps and two spring tides. Dissipation is averaged arithmetically, not logarithmically, and the color scale for the dissipation is correspondingly higher.

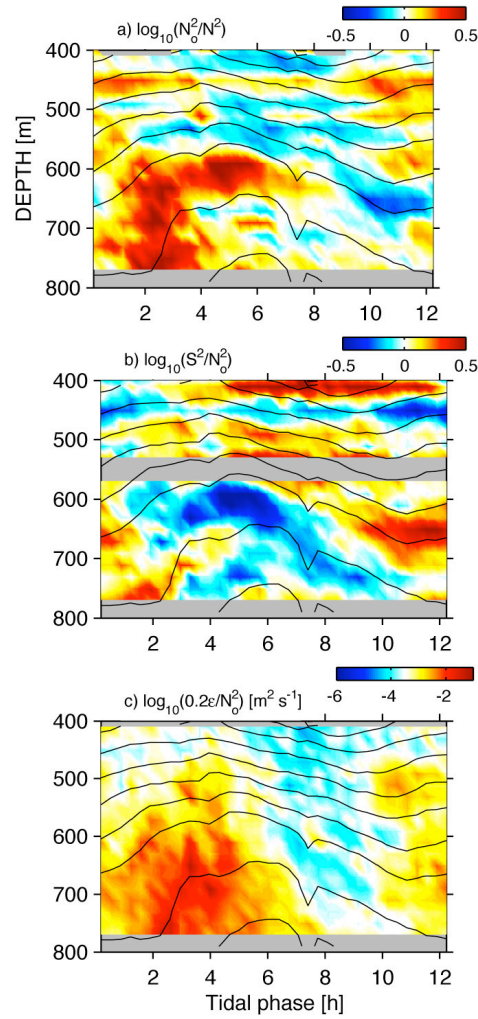


FIG. 16. Tidal phase-averaging for the second spring tide ($t = 0$ is slack barotropic flow before the on-ridge phase). a) stratification anomaly, b) shear anomaly, and c) diffusivity (dissipation from potential-density overturns scaled by stratification). The dissipation varies by almost two orders of magnitude as the phase changes. The strain is very large where the turbulence is the highest.

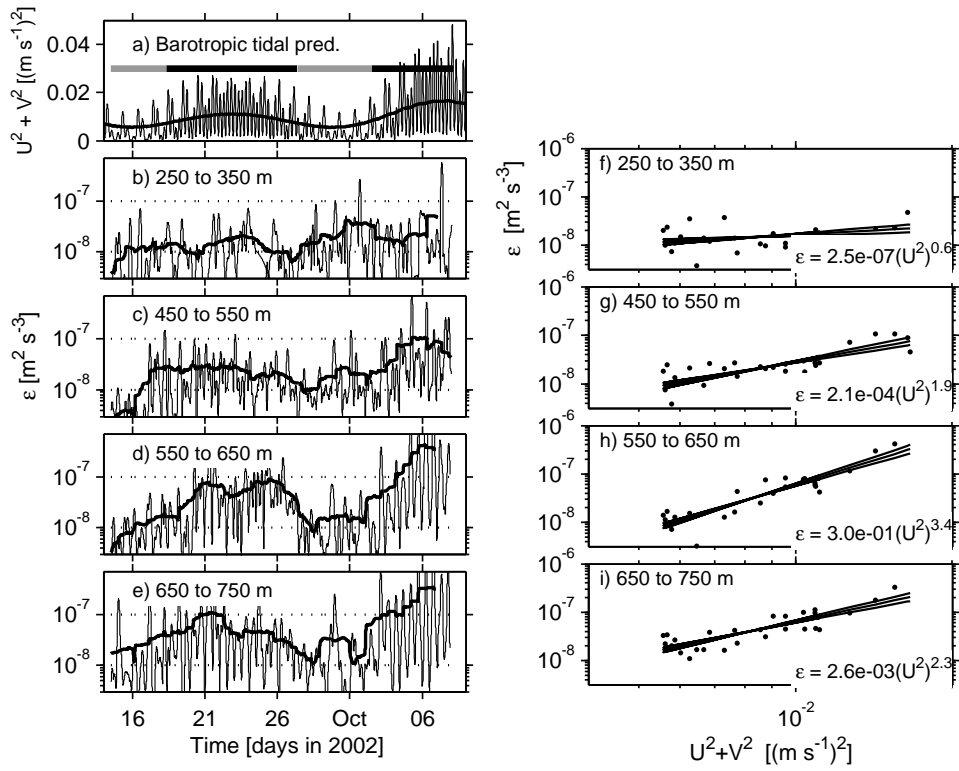


FIG. 17. a) Square of the predicted tidal velocity (thin), and smoothed by 4-tidal periods (thick). b) Mean dissipation (ϵ_p) between 250-350 m, smoothed by four tidal periods (thick), and a quarter tidal period (thin). c)–e) 100-m bins going down in depth. f)–i) are the smoothed dissipation versus the smoothed tidal velocities (slightly oversampled at 2 tidal periods). The dissipation is fit as a power law to the tidal amplitude squared.

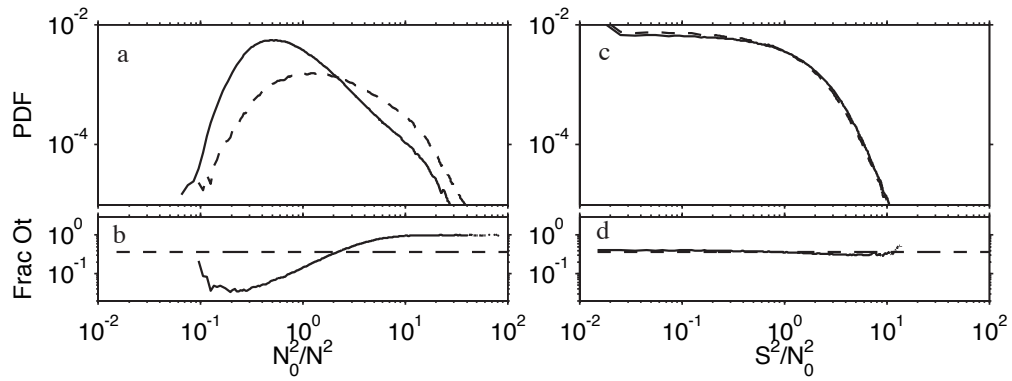


FIG. 18. a) PDF of strain (solid), and strain where there are overturns (dashed). b) Fraction of water column overturning in each strain bin. Dashed line is total fraction overturning in the water column. c) and d) same, except for shear. Data is from 450-750 m, during the first spring tide.

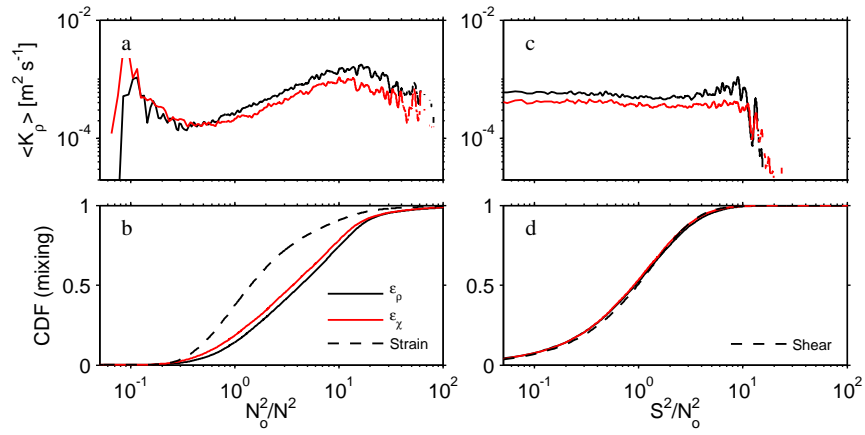


FIG. 19. From the first spring tide: a) mean dissipation ($K_p = 0.2\varepsilon N_0^{-2}$) as a function of strain, using both ε_p (black) and ε_χ (red) b) CDF of K_p (black and red) and strain (dashed). c) and d) as (a) and (b), for shear.

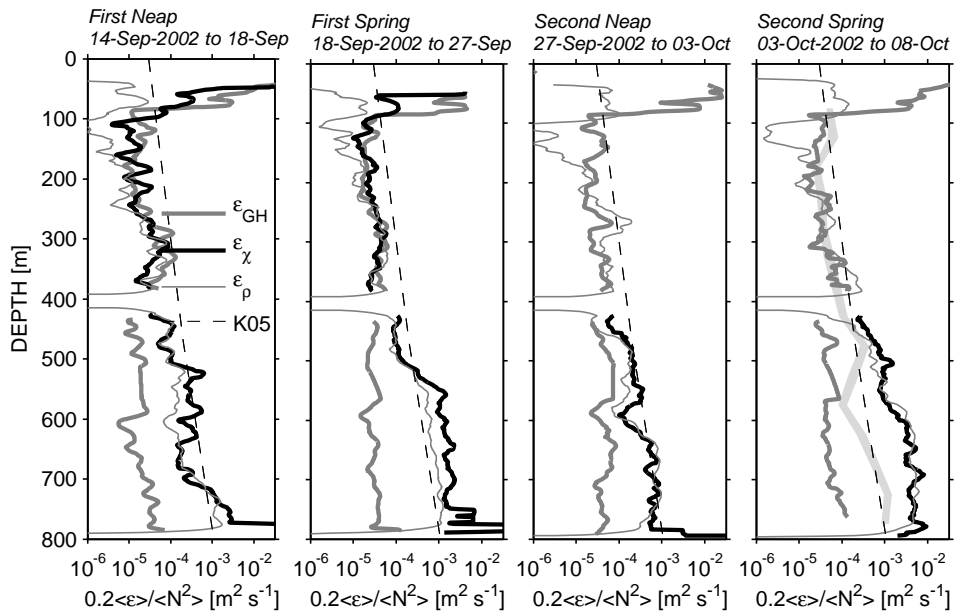


FIG. 20. Average vertical profiles of turbulence dissipation, normalized by mean stratification (to make a diapycnal diffusivity) for the four time periods. Thick black line is the estimate from the microconductivity probe; thin shaded line from density overturns; thick shaded line from Gregg-Henyey parameterization (equation (7)). There was no microconductivity from the upper CTD for the second two time periods. The dashed line is the composite dissipation profile from direct turbulence measurements made in deep water atop the ridge (Klymak et al. 2006). The light-shaded band in the last panel is the actual average profile from (Klymak et al. 2006). (Fig. 2),

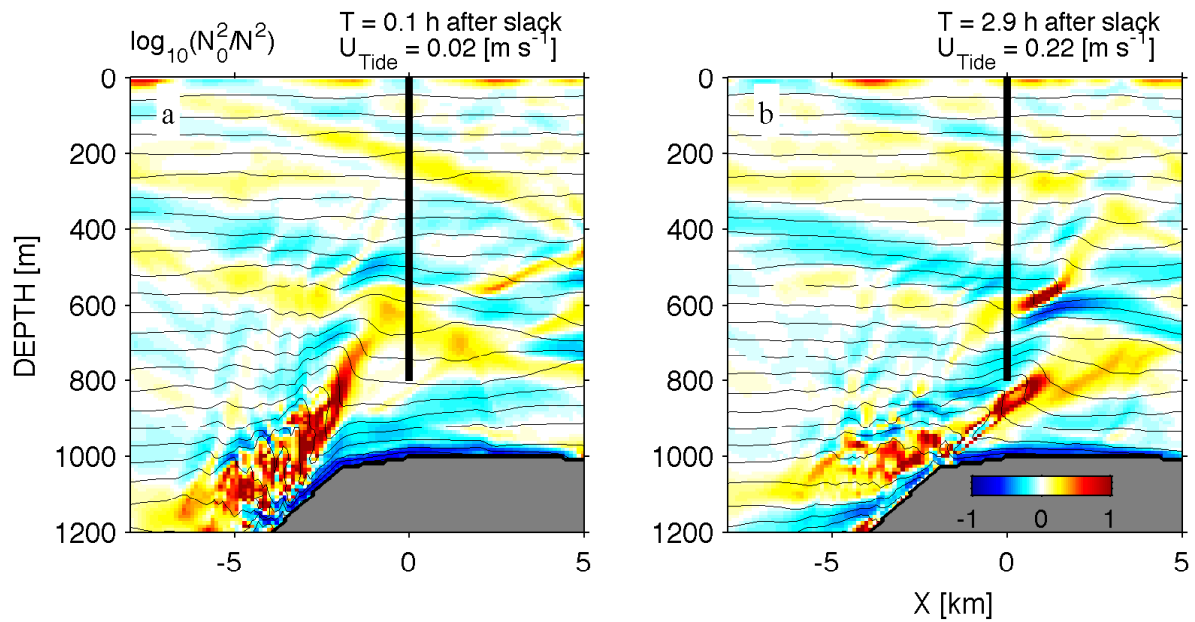


FIG. 21. Strain fields in a two-dimensional numerical simulation of barotropic flow over the ridge (Legg and Klymak 2007) for a) slack tide and b) after 3 h of on-ridge flow. The high-strain at 600 m, and deeper than 750 m is similar to that observed at FLIP. It originates near the ridge break (a) and propagates on-ridge as the tide switches from off-ridge to on-ridge (b).